Integrating computational chemistry and machine learning to predict KRAS mutation-induced resistance

Katarzyna Mizgalska[1,2], Konstancja Urbaniak[3], Denis J. Imbody[4], Eric B. Haura[4], Wayne C. Guida[2], Sergio Branciamore[3], Aleksandra Karolak[1]

[1]Department of Machine Learning, Moffitt Cancer Center, Tampa, FL, United States of America

[2]Department of Chemistry, University of South Florida, Tampa, FL, United States of America

[3]Department of Computational and Quantitative Medicine, City of Hope, Monrovia, CA, United States of America

[4]Department of Thoracic Oncology, Moffitt Cancer Center, Tampa, FL, United States of America

*Corresponding author: Aleksandra Karolak (AK)

aleks.karolak@moffitt.org

Abstract

Mutation-induced drug resistance is a major contributor to the failure of targeted cancer therapies, particularly in tumors driven by mutations in the KRAS oncogene. Although covalent inhibitors effectively target KRAS G12C, secondary mutations such as G12C/Y96C, G12C/Y96S, and G12C/Y96D lead to resistance despite leaving the covalent attachment site intact. To predict these resistance outcomes, we developed a computational framework that integrates molecular dynamics-derived structural, energetic, thermodynamic, and contact-based descriptors with machine learning. Features extracted from simulations of treatment-sensitive and treatment-resistant KRAS mutants were used to train logistic regression, random forest, support vector machine, and Bayesian Network classifiers, achieving average accuracies above 90%. Solvent-accessible surface area variability, Lennard-Jones 1,4 energy, mean square displacement, and root mean square fluctuation emerged as the most discriminatory features. Residues G10, E62, and H95 showed the highest predictive value. This approach highlights conformational and solvent-exposure changes as central drivers of KRAS drug resistance and provides a generalizable workflow for other clinically relevant mutant targets.

Author Summary

Mutation-induced resistance is a common challenge across many cancer types and is often associated with aggressive tumor progression and poor therapeutic response. Investigating the dynamic properties of proteins harboring such mutations provides valuable insights into the structural and functional consequences of these alterations, thereby helping to elucidate the mechanisms of drug resistance. Machine learning algorithms are particularly effective at uncovering complex patterns within high-dimensional data, such as molecular dynamics simulation trajectories. Integrating these algorithms with analysis of protein dynamics holds significant potential to aid in drug discovery challenges by reducing both time and resource demands while increasing the likelihood of identifying effective therapeutic candidates.

As a proof of concept, we developed a computational framework that integrates molecular dynamics-derived molecular features with machine learning to distinguish treatment-sensitive from treatment-resistant KRAS mutants. KRAS is known for drug resistance arising from secondary mutations that disrupt inhibitor binding despite intact covalent attachment sites. The models achieved over 90% accuracy and identified solvent-exposure and conformational changes at residues G10, E62, and H95 as key predictors of treatment resistance. This workflow offers a generalizable strategy for understanding and forecasting mutation-induced resistance.

Introduction

Mutation-induced drug resistance presents a major challenge in cancer therapy, particularly for targeted treatments. Such resistance can arise through various mechanisms [1], including activation of alternative signaling pathways, eg, BRAF(V600E) inhibition by vemurafenib in colon cancer [2]; impaired apoptosis, as seen in p53(R273W) resistance to 5-fluorouracil [3]; and enhanced DNA repair, eg, BRCA1/2 reversion mutations conferring resistance to polyadenosine diphosphate ribose polymerase inhibitors [4]. This study focuses on a common mechanism of resistance driven by direct mutations in the drug target itself. Such mutations frequently alter the chemical and conformational properties of the target, often within the binding site, disrupting drug-receptor interactions. This mechanism, among others, is especially concerning for one of the most frequently mutated oncogenes, Kirsten rat sarcoma viral oncogene homolog (*KRAS*) [5, 6].

The *KRAS* oncogene encodes a 21 kDa guanosine triphosphate hydrolase (GTPase) K-Ras (KRAS henceforward) that regulates key signaling pathways involved in cell-cycle control [6, 7]. Structurally, KRAS consists of a G-domain (residues 1–166), which binds guanine nucleotides, and a hypervariable region (residues 167–189), which mediates membrane association [7]. Its secondary structure includes 6 β-sheets and 5 α-helices connected by flexible loops. Important regions (shown in **Fig 1**) include the switch I and switch II loops, which interact with effector and regulatory proteins, and the P-loop, which binds nucleotide phosphate groups [7]. KRAS homolog alternates between an inactive guanosine diphosphate– (GDP) bound and an active guanosine triphosphate– (GTP-) bound state. Guanine nucleotide exchange factors (GEFs) promote the release of GDP, allowing GTP, which is more abundant in the cell, to bind and

78 stabilize the active conformation [8]. Binding of GTP activates KRAS by inducing
79 conformational changes in the switch I and switch II loops. The activated protein then engages
80 downstream signaling pathways, including the mitogen-activated protein kinase (MAPK)
81 pathway, the Ras-like small GTPases pathway, and the phosphoinositide-3-kinase pathway,
82 which are critical regulators of cell proliferation, survival, growth, and differentiation [9].
83 Termination of signaling requires GTP hydrolysis, facilitated by GTPase-activating proteins,
84 returning KRAS to its inactive state [8].

85 Mutations in signaling pathways such as Ras/Raf/MAPK are frequently implicated in cancer,
86 with KRAS being one of the most commonly mutated oncogenes [6] accounting for 11.6% of all
87 carcinomas [5]. In pancreatic ductal adenocarcinoma, KRAS mutations are present in 81.7% of
88 cases, with G12D as the predominant subtype [5]. In colorectal cancer, KRAS mutations occur in
89 38% of patients, primarily G12D and G12V[5], while in non–small-cell lung cancer, the
90 prevalence is 21.2%, with G12C representing 45% of cases [5, 6, 10, 11]. Point mutations at
91 KRAS residues G12, G13, and Q61 impair GAP-mediated GTP hydrolysis, leading to
92 constitutive KRAS activation and tumorigenesis [12].

93 Until recently, KRAS-driven tumors were considered difficult to treat because of KRAS's
94 picomolar affinity for GTP and the absence of other druggable pockets on its surface. As a result,
95 therapeutic strategies focused on targeting KRAS indirectly [13, 14]. A breakthrough came in
96 2013, when Ostrem et al [15] reported the first covalent inhibitor targeting the KRAS G12C
97 mutant. The compound bound specifically to a cysteine residue within an allosteric pocket
98 located beneath the switch II region in the inactive (GDP-bound) KRAS conformation. This
99 breakthrough led to the development of the first KRAS G12C inhibitors approved for clinical
100 use. In 2021, AMG510 [16] (sotorasib, Lumakras) was approved by the FDA for treating non–

101 small-cell lung cancer, followed by MRTX849 [17] (adagrasib, Krazati) in 2022. Both drugs
102 irreversibly bind to the cysteine residue at position 12 and form noncovalent interactions with
103 other amino acids in the switch II binding site, including tyrosine (Y96), glutamine (Q99), and
104 histidine (H95). This interaction network stabilizes the inactive, GDP-bound conformation of
105 KRAS, thereby inhibiting oncogenic signaling [18, 19].

106 Despite initial clinical success, resistance to sotorasib and adagrasib has emerged through
107 various mechanisms [20, 21]. One involves RTK-mediated activation of wild-type RAS [22].
108 Another features secondary mutations in KRAS G12C, such as Y96D [23-25], Y96S [24,
109 25], and Y96C [24, 26], which confer resistance to both approved drugs. Other mutations, such
110 as G12C/G13D, R68M, A59S, and A59T, are resistant to sotorasib alone, while Q99L is
111 associated with resistance to adagrasib [24, 25]. These secondary mutations reactivate ERK
112 signaling and are likely to promote broader resistance across tumor-cell populations [27].

113 Current efforts to target KRAS-driven tumors include inhibitors of GDP-bound KRAS G12C and
114 G12D, as well as proteolysis-targeting chimeras for KRAS G12D and G12V, all in clinical trials
115 [28]. Alternative strategies focus on the active, GTP-bound form of KRAS and binding regions
116 outside of switch II to circumvent resistance from secondary mutations [29]. However, the
117 molecular basis of resistance arising in the inactive-state binding site, particularly in KRAS
118 secondary mutants, remains poorly understood, underscoring the potential benefit of targeted
119 approaches against these specific variants.

120 This study moves beyond prevailing studies focused on conformational analyses [30], single
121 KRAS mutants [31-33] or drug design [34]. Instead, we investigate the underlying factors of
122 mutation-induced resistance caused by secondary mutations in the KRAS switch II binding site:

123 KRAS G12C/Y96D, G12C/Y96C, and G12C/Y96S, which exhibit resistance to both sotorasib
124 and adagrasib. As both drugs interact with residue Y96 [19], substitution at this site represents a
125 direct structural change relative to the G12C single mutant, which may influence drug binding.
126 However, other molecular features may also contribute to resistance. To address this, we
127 developed a framework combining molecular dynamics– (MD-) derived descriptors with
128 machine learning (ML) algorithms to identify features that differentiate treatment-resistant
129 KRAS mutants from treatment-sensitive ones.

130 Integrating dynamic properties of biological systems with ML offers a novel approach to
131 tackling complex challenges in drug discovery [35]. While some studies have incorporated MD
132 descriptors into ML models, they have primarily focused on ligand-based pharmacophore
133 analyses [36], without accounting for protein or binding site dynamics. Other approaches
134 describe protein-binding sites statically and apply ML to support ligand design [37]. Although a
135 few efforts have incorporated protein flexibility and ML, eg, to identify druggable binding sites
136 [37-39], this approach has not yet been applied to address complex problems such as mutation-
137 induced drug resistance.

138 Results

139 This study investigated mutation-induced drug resistance using the KRAS oncogene as a case
140 study. Based on experimental treatment responses, KRAS structures were classified either as
141 treatment-sensitive (G12C) or treatment-resistant (G12C/Y96C, G12C/Y96S, and G12C/Y96D).
142 Because the secondary mutations occur within the switch II binding site, we first assessed
143 structural differences in this region using SiteMap (**Fig 1**). One key output, SiteScore, reflects the
144 likelihood of small-molecule binding, with values near 1 indicating promising binding

145 sites. KRAS WT exhibited a shallow switch II pocket with a low SiteScore (0.754) and small
146 volume (123 $Å^3$), suggesting unlikely small-molecule binding, consistent with the absence of
147 endogenous ligands in native KRAS. In contrast, the G12C single mutant and all secondary
148 mutants had a SiteScore near 1, but their binding pocket volumes varied: G12C had a smaller
149 volume (256 $Å^3$), while the secondary mutants ranged from 325 to 353 $Å^3$. This volume increase
150 is likely attributable to substitution of bulky tyrosine at position 96 with smaller residues
151 (cysteine, serine, or aspartic acid).

152 **Fig 1**. **KRAS mutation points and SiteMap analysis**. The first row shows labeled structural
153 elements of KRAS forms; the second row shows their respective switch II binding sites. Binding
154 site properties: binding site surface (cyan), hydrogen bond donors (blue), hydrogen bond
155 acceptors (red), hydrophobic surface (yellow), and GDP (orange). The binding SiteScore and
156 volume are reported next to each molecule. For visualization purposes, switch II is approximated
157 on residues 58–72, switch I on residues 30–40, and P-loop on residues 10–14 as suggested in the
158 following work [7]. The visualizations were prepared with PyMOL Molecular Graphics System
159 [40]. Abbreviations: GDP, guanosine diphosphate; KRAS, Kirsten rat sarcoma viral oncogene
160 homolog. Corresponding PDB structures include 6MBT (KRAS WT); 6OIM (KRAS G12C);
161 6OIM manually mutated (KRAS G12C/Y96C/D/S).

162 To capture dynamic and subtle structural changes not evident from static analysis, we performed
163 MD simulations of each KRAS mutant in the absence of inhibitors. From the MD trajectories,
164 we extracted a comprehensive set of molecular descriptors reflecting global structural behavior
165 and localized changes within key regions of the protein. These features were categorized into 4
166 groups: structural, energetic, thermodynamic, and intra/intermolecular contacts. The descriptors
167 most strongly associated with resistance were related to the site of secondary mutation (residue

168 96), and the average solvent-accessible surface area (SASA) of residues G10 and A11. After
169 removing highly intercorrelated variables (see Methods section), the remaining features were
170 subjected to statistical and ML analyses.

171 Univariate statistical analysis

172 The RMSD relative to the reference structure was calculated to assess system stability. Protein
173 backbone RMSD plots (**Fig 2**) illustrate structural fluctuations in treatment-sensitive and
174 treatment-resistant KRAS systems throughout the simulation. The treatment-sensitive systems
175 reached a maximum RMSD of 0.41 nm (**Fig 2A**), while the treatment-resistant systems exhibited
176 greater protein fluctuations, with RMSD values rising to 0.50 nm (**Fig 2B**). To better
177 characterize this variability, we generated violin plots of backbone RMSD distributions for the
178 most populated conformations (**Fig 2C**). In both groups, medians were broadly distributed
179 around similar values (0.20 and 0.21 nm), although the treatment-resistant group exhibited
180 greater variability than the treatment-sensitive group (RMSD range: 0.13–0.39 nm vs 0.13–
181 0.32 nm). However, the Mann–Whitney U test revealed no statistically significant difference (*P*
182 value >.05) in backbone RMSD distributions between groups.

183 Among all RMSD-based features, only the RMSD of the backbone–GDP complex showed a
184 statistically significant difference (**Table 1**). While both groups displayed values concentrated
185 near their medians (0.12 and 0.09 nm, **Fig 2D**), the treatment-sensitive systems were shifted
186 toward higher RMSD values (mean: 0.13 vs 0.11 nm, mean values not shown) than treatment-
187 resistant systems, suggesting their greater structural flexibility regarding the protein–GDP
188 complex.

189 **Fig 2. RMSD over the molecular dynamics simulation.** (**A**) KRAS treatment-sensitive

190 systems. (**B**) KRAS treatment-resistant systems. Data distribution of structural features with

191 annotated median and *P* values. (**C**) Protein backbone RMSD. (**D**) Protein backbone–GDP

192 RMSD. (**E**) Protein backbone MSD of switch II binding site residues. (**F**) Protein Rg.

193 Abbreviations: GDP, guanosine diphosphate; KRAS, Kirsten rat sarcoma viral oncogene

194 homolog; MSD, mean square deviation; RMSD, root mean square deviation.

195 **Table 1. The results of Mann–Whitney U test**. Molecular features with *P* value less than 0.05.

Molecular feature	P-value
SASA G10 SD*	1.50×10^{-17}
SASA H95 AV*	1.75×10^{-12}
LJ 1,4	2.19×10^{-8}
SASA E62 SD	6.00×10^{-8}
RMSF M72	1.20×10^{-7}
SASA I100 AV	1.35×10^{-7}
SASA V103 SD	1.46×10^{-7}
SASA V9 AV	1.83×10^{-7}
SASA Q99 AV	4.72×10^{-6}
SASA K16 AV	1.44×10^{-5}
RMSF Q99	1.64×10^{-5}
RMSF H95	2.83×10^{-5}
RMSF Y64	4.62×10^{-5}
Hb protein-GDP	2.59×10^{-4}
SASA V9 SD	4.20×10^{-4}
SASA M72 SD	4.75×10^{-4}
RMSF I100	5.61×10^{-4}
RMSD backbone-GDP	1.37×10^{-3}
Entropy quasi-harmonic	1.47×10^{-3}
SASA G60 AV	1.99×10^{-3}
SASA D69 SD	2.61×10^{-3}
SASA protein	3.06×10^{-3}
RMSF Q61	3.16×10^{-3}
Coulomb 1,4	3.64×10^{-3}
RMSF D69	3.72×10^{-3}
SASA C12 AV	4.45×10^{-3}
RMSF G10	7.66×10^{-3}
MSD bs*-backbone	1.01×10^{-2}
RMSF E63	1.19×10^{-2}
SASA E63 AV	1.77×10^{-2}

SASA Q61 SD	1.94×10^{-2}
SASA H95 SD	2.22×10^{-2}
Rg protein	2.69×10^{-2}
SASA D69 AV	4.65×10^{-2}
SASA T35 SD	4.84×10^{-2}

*Abbreviations: AV, per average; bs, switch II binding site.

Another statistically significant feature associated with structural displacement was the mean square displacement (MSD) of the switch II binding site backbone (**Fig 2E**, **Table 1**). Like the protein–GDP complex, the MSD distribution for the switch II binding site backbone was shifted toward higher values in the treatment-sensitive systems (median: 4.82 vs 4.47 nm²) and showed greater variability (mean 4.73 nm² ± 0.86 nm² vs. 4.39 nm² ± 0.77 nm²), compared with the treatment-resistant group. This indicates that, on average, backbone atoms in the switch II binding region moved farther from their reference positions in the treatment-sensitive systems. In contrast, the radius of gyration (Rg), a measure of a protein compactness, showed a slight increase in the treatment-resistant group values compared to the treatment-sensitive systems (median: 1.57 with max Rg: 1.61 nm vs 1.56 and 1.59 nm, **Fig 2F**). Although the magnitude of this difference was small, it yielded a *P* value marginally below .05, suggesting borderline statistical significance.

Unlike global RMSD, which captures overall structural deviation, root mean square fluctuation (RMSF) provides insight into residue-level flexibility. **Figs 3A-B** shows RMSF values across the entire simulation time, with arrows marking peaks above 0.4 nm to highlight the most flexible residues. In both groups, residues T35, E63, and Y64 consistently exhibited the highest peaks. Additionally, P34 and E62 showed increased fluctuations in the treatment-sensitive systems, while E37 and Q61 showed higher flexibility in the treatment-resistant group. Among these, only Q61, E63, and Y64 exhibited statistically significant RMSF differences between groups (**Table 1**). Analysis of the most populated conformations revealed additional switch II binding site

218 residues with significant group-wise RMSF differences, including M72, Q99, H95, I100, D69,
219 and G10 (**Fig 3C**). For 8 out of the 9 reported residues, the treatment-resistant group had higher
220 median RMSF values than the treatment-sensitive group, indicating greater structural flexibility.

221 **Fig 3. RMSF over the molecular dynamics simulation**. Residues with RMSF >0.4 nm are
222 indicated with arrows. (**A**) KRAS treatment-sensitive systems. (**B**) KRAS treatment-resistant
223 systems. (**C**) RMSF data distribution for the individual residues in the switch II binding site
224 ranked by the lowest *P* value, with annotated median values. Abbreviations: KRAS, Kirsten rat
225 sarcoma viral oncogene homolog; RMSF, root mean square deviation.

226 The final structural feature analyzed was SASA. Regarding the total SASA of the protein in the
227 most populated conformations, treatment-resistant systems exhibited slightly higher values
228 (median: 97.45 nm^2) compared with treatment-sensitive systems (95.95 nm^2), indicating
229 increased solvent exposure, statistically significant between groups (**Table 1**). To gain residue-
230 level insight, SASA was further analyzed within the switch II binding site. Violin plots in
231 **Figs 4A-B** highlight the top 5 residues with the lowest *P* values for both average (AV) and SD of
232 SASA. Across these residues, median SASA values were consistently higher in the treatment-
233 resistant group, suggesting increased solvent exposure. The most significant difference was
234 observed in the SASA (SD) for residue 10 ($P = 1.5 \times 10^{-17}$), followed by the SASA (AV) of
235 residue 95 ($P = 1.8 \times 10^{-12}$) and the SASA (SD) for residue 62 ($P = 6 \times 10^{-8}$), highlighting
236 substantial variation in solvent accessibility between groups at the individual residue level.

237 The next group of features included energetic properties: potential energy, kinetic energy, and
238 both short-range and 1,4 Coulomb and Lennard-Jones (LJ) interaction energies. Among these, LJ
239 1,4 energy and Coulomb 1,4 energy showed statistically significant differences between

240 treatment-sensitive and treatment-resistant groups (**Table 1**). Lennard-Jones 1,4 energy had the
241 third lowest *P* value among all features, with consistently higher values in the treatment-sensitive
242 group (median: 2075 mean: 2077 kJ/mol) compared with the treatment-resistant group (2032 and
243 2031 kJ/mol), highlighting the difference in nonbonded interactions energies between the groups
244 (**Fig 4C**). Conversely, Coulomb 1,4 energy was significantly elevated in the treatment-resistant
245 systems (median: 23 369 vs 23 234 kJ/mol, data not shown).

246 To gain insight into thermodynamic properties of the systems, enthalpy and entropy were
247 analyzed. Entropy calculated using the quasiharmonic approximation showed a statistically
248 significant difference between treatment-sensitive and treatment-resistant groups (**Table 1**, **Fig**
249 **4D**) with elevated values in the treatment-resistant systems (median: 3485 vs 3434 and mean:
250 3507 vs 3407 kJ/mol). This finding aligns with the generally increased conformational flexibility
251 in the treatment-resistant group, as indicated by structural features such as RMSF and SASA.

252 Intra- and intermolecular contacts were also analyzed. Intramolecular interactions included
253 contacts between the protein and individual amino acid residues, as well as hydrogen bond
254 formation within the protein. Intermolecular interactions focused on hydrogen bonds formed
255 between the protein and GDP. The first group of contacts included residue 12, as cysteine at this
256 position serves as the covalent binding partner for small-molecule inhibitors targeting the KRAS
257 G12C mutant. A higher number of contacts between C12 and the rest of the protein were
258 observed in the treatment-sensitive systems, compared with the treatment-resistant ones (median:
259 41 vs 37, **Fig 4E**); however, this difference was not statistically significant. Among hydrogen
260 bond–related features, the number of protein-GDP hydrogen bonds differed significantly
261 between the 2 groups (**Table 1**). The treatment-resistant systems exhibited a higher median
262 hydrogen bond count (median:10, range 8-13) than the treatment-sensitive group (9 and range 7-

263 14), indicating more frequent protein-GDP interactions in the treatment-resistant group on
264 average, although the treatment-sensitive group exhibited a more disperse range (**Fig 4F**). This
265 finding is correlated to more stable GDP binding pocket in treatment-resistant group (**Fig 2D**),
266 which allows for more stable occurrence of hydrogen bonds on average. It was reported in
267 previous studies [30] that both stronger and weaker GDP binding is possible for KRAS
268 secondary mutants.

269 Statistical analysis suggested that the relationships between molecular features are complex, with
270 no single trend consistently distinguishing the 2 groups. For instance, the treatment-resistant
271 systems showed increased flexibility in the switch II binding site region, as indicated by RMSF
272 and SASA, while the treatment-sensitive systems exhibited greater mobility in the same region's
273 backbone, as measured by MSD. These complex findings highlight the structural variability at
274 the residue level, making it challenging to draw definitive conclusions about the overall direction
275 or significance of individual features.

276 **Fig 4. Data distribution of structural features, thermodynamic features and intra- and**
277 **intermolecular contacts with annotated median and *P* values.** (**A**) SASA (AV) of the switch
278 II binding site residues ranked by the lowest *P* value. (**B**) SASA (SD) for the switch II binding
279 site residues ranked by the lowest *P* value. (**C**) LJ 1,4 energy. (**D)** Entropy calculated according
280 to the quasiharmonic equation. (**E**) Intramolecular contacts count between C12 and the rest of
281 protein residues. (**F**) Hydrogen bonds count between the protein residues and GDP.
282 Abbreviations: GDP, guanosine diphosphate; LJ, Lennard-Jones; SASA, solvent-accessible
283 surface area.

Machine-learning models

Given the complexity of MD simulations data, we applied ML to uncover multivariate patterns that may not be apparent through univariate analysis alone, and to identify the most informative features capable of distinguishing treatment-resistant mutants from treatment-sensitive ones (**Fig 5A**). All predictive ML models (LR, RF, and SVM), achieved high classification performance, with average accuracy and area under the curve exceeding 90% (**Table 2**, **Fig 5B**). Model stability across methods was confirmed through 10-fold cross-validation. Hyperparameter tuning using GridSearchCV yielded parameter values close to the defaults (**Table 2**), further indicating robust and generalizable performance.

Across all ML models, the SASA (SD) for residue G10 (**Fig 5A**) was consistently ranked as the most predictive feature differentiating treatment-resistant from treatment-sensitive KRAS systems. This result aligns with the Mann–Whitney U test, where this feature had the lowest *P* value among all descriptors, indicating the strongest statistical significance. The SASA (SD) for residue G10, was elevated in treatment-resistant systems (**Fig 4B**), along with its RMSF, which was also statistically significant (**Table 1**).

Fig 5. Machine-learning analyses. (**A**) The top important features selected by the machine learning models: LR, RF, and SVM, ranked in the descending order by mean importance, normalized on a 0 to 1 scale. (**B**) Performance of the ML models. ROC AUC curves for LR, RF, and SVM models. (**C**) BN: a subset of the network highlighting the top features is shown. Node colors correspond to the state of each feature when the *resistance* node is fixed to state 1, with red indicating higher marginal value and blue indicating lower marginal value. (**D**) Comparison of how different feature-state combinations influence the likelihood of treatment resistance

307 outcome in BN. Each cell shows the marginal probability of treatment resistance when a specific

308 molecular descriptor is fixed at a given state (0, low; 1, medium; and 2, high). Abbreviations:

309 AUC, area under the curve; BN, Bayesian network; LR, logistic regression; ML, machine

310 learning; RF, random forest; ROC, receiver-operating characteristic; SVM, support vector

311 machine.

312 **Table 2. Performance of the ML Models.** Logistic Regression (LR), Random Forest (RF) and
313 Support Vector Machine (SVM) in terms of standard metrics: accuracy, precision, recall, area
314 under the curve and specificity. Evaluated using 10-fold cross-validation.

Logistic Regression[a]															
Metric	**Accuracy**			**Precision**			**Recall**			**AUC**			**Specificity**		
Run	**Regularization method**														
	L2	L1	Elastic Net	L2	L1	Elastic Net	L2	L1	Elastic Net	L2	L1	Elastic Net	L2	L1	Elastic Net
1	0.962	0.923	0.885	0.923	0.857	0.800	1.000	1.000	1.000	1.000	0.863	0.887	0.929	0.857	0.786
2	0.962	1.000	0.962	1.000	1.000	1.000	0.909	1.000	0.909	1.000	1.000	1.000	1.000	1.000	1.000
3	0.923	0.962	0.962	0.846	0.917	0.917	1.000	1.000	1.000	0.982	0.933	0.933	0.867	0.933	0.933
4	1.000	0.962	0.962	1.000	0.917	0.917	1.000	1.000	1.000	1.000	0.945	0.976	1.000	0.933	0.933
5	0.885	0.923	0.923	0.786	0.846	0.846	1.000	1.000	1.000	0.933	0.867	0.867	0.800	0.867	0.867
6	1.000	0.923	0.923	1.000	0.875	0.875	1.000	1.000	1.000	1.000	0.917	0.940	1.000	0.833	0.833
7	0.846	0.962	0.962	0.929	1.000	1.000	0.813	0.938	0.938	0.944	1.000	0.994	0.900	1.000	1.000
8	0.923	0.962	0.962	0.923	0.929	0.929	0.923	1.000	1.000	0.994	0.923	0.929	0.923	0.923	0.923
9	0.962	0.962	1.000	1.000	0.917	1.000	0.909	1.000	1.000	0.958	1.000	1.000	1.000	0.933	1.000
10	1.000	0.923	0.923	1.000	0.882	0.882	1.000	1.000	1.000	1.000	0.824	0.836	1.000	0.818	0.818
Average ±SD	0.946 ± 0.052	0.950 ± 0.026	0.947 ± 0.032	0.941 ± 0.076	0.914 ± 0.053	0.917 ± 0.069	0.955 ± 0.065	0.994 ± 0.020	0.985 ± 0.033	0.981 ± 0.026	0.927 ± 0.062	0.936 ± 0.058	0.942 ± 0.071	0.910 ± 0.064	0.909 ± 0.080

Random Forest[b]										
Run	**Parameters**									
	Default	Optimized	Default	Optimized	Default	Optimized	Default	Optimized	Default	Optimized
1	0.885	0.885	0.800	0.800	1.000	1.000	0.940	0.935	0.786	0.786
2	0.962	1.000	1.000	1.000	0.909	1.000	1.000	1.000	1.000	1.000
3	0.923	0.923	0.846	0.846	1.000	1.000	0.988	0.982	0.867	0.867
4	0.962	0.962	0.917	0.917	1.000	1.000	1.000	1.000	0.933	0.933
5	0.808	0.808	0.688	0.688	1.000	1.000	0.948	0.942	0.667	0.667
6	0.962	0.962	0.933	0.933	1.000	1.000	0.988	0.973	0.917	0.917
7	0.885	0.923	1.000	1.000	0.813	0.875	0.984	0.975	1.000	1.000
8	0.962	0.962	0.929	0.929	1.000	1.000	0.964	0.950	0.923	0.923
9	1.000	1.000	1.000	1.000	1.000	1.000	1.000	1.000	1.000	1.000
10	0.923	0.923	0.882	0.882	1.000	1.000	0.967	0.973	0.818	0.818
Average ±SD	0.927 ± 0.056	0.935 ± 0.057	0.899 ± 0.100	0.899 ± 0.100	0.972 ± 0.063	0.988 ± 0.040	0.978 ± 0.022	0.973 ± 0.024	0.891 ± 0.109	0.891 ± 0.109

Support Vector Machine[c]										
Run	**Parameters**									
	Default	Optimized	Default	Optimized	Default	Optimized	Default	Optimized	Default	Optimized
1	0.885	1.000	0.800	1.000	1.000	1.000	0.982	1.000	0.786	1.000
2	1.000	1.000	1.000	1.000	1.000	1.000	1.000	1.000	1.000	1.000
3	0.885	0.885	0.786	0.786	1.000	1.000	0.988	0.994	0.800	0.800
4	0.962	0.962	0.917	0.917	1.000	1.000	1.000	0.994	0.933	0.933
5	0.808	0.885	0.688	0.786	1.000	1.000	0.921	0.958	0.667	0.800

6	0.962	0.962	0.933	1.000	1.000	0.929	1.000	1.000	0.917	1.000
7	0.962	0.846	1.000	0.929	0.938	0.813	0.963	0.913	1.000	0.900
8	0.962	0.923	0.929	0.923	1.000	0.923	0.994	0.994	0.923	0.923
9	0.962	0.962	0.917	1.000	1.000	0.909	1.000	0.933	0.933	1.000
10	0.923	1.000	0.882	1.000	1.000	1.000	0.952	1.000	0.818	1.000
Average ±SD	0.931 ± 0.057	0.942 ± 0.055	0.885 ± 0.099	0.934 ± 0.086	0.994 ± 0.020	0.957 ± 0.063	0.980 ± 0.027	0.979 ± 0.032	0.878 ± 0.107	0.936 ± 0.081

[a]**Logistic regression parameters**:

- **L2**: 'C': 1.0, solver: lbfgs (default parameters)
- **L1:** best parameters from GridSearchCV: 'C': 0.1, solver:saga
- **Elastic Net:** best parameters from GridSearchCV: 'C': 0.1, 'l1_ratio': 0.5, solver:saga

[b]**Random forest parameters**:

- **Default**: n_estimators=100, max_depth=None, min_samples_split=2, min_samples_leaf=1,max_features='auto'
- **Optimized:** best parameters from GridSearchCV: n_estimators: 50, max_depth: None, max_features: 'sqrt', min_samples_leaf: 1, min_samples_split: 2

[c]**Support vector machine parameters**:

- **Default:** C: 1.0, gamma: 'scale' kernel: 'rbf'
- **Optimized**: best parameters from GridSearch:C: 100, gamma: 0.001, kernel: 'rbf'

Other top-ranked features included the SASA (AV) for H95 and the SASA (SD) for E62, both of which also had among the lowest *P* values. The SASA (AV) for H95 was notably higher in treatment-resistant systems, similar to the residue G10 (**Fig 4A**). In contrast, the SASA (SD) for E62 was elevated in treatment-sensitive systems (**Fig 4B**). Additionally, its RMSF showed high discriminatory power in the LR model, further highlighting its contribution to conformational dynamics relevant to treatment response.

Additional features prioritized by the models included LJ 1,4 energy, the SASA (AV) of K16, and the MSD of the switch II binding site backbone. All were statistically significant, with LJ 1,4 energy ranked as the third most significant feature overall. LJ 1,4 energy values and MSD of the switch II binding site backbone were both more concentrated at higher levels in the treatment-sensitive systems (**Figs 4C and 2E**, respectively), whereas the SASA (AV) of K16 was elevated in the treatment-resistant systems (**Fig 4A**). For validation, we ran two additional ML models (XGBoost and PLS-DA), which remained in agreement with the results. Models' performance and evaluation can be found in the Supplementary Material (**S1 and S2 Tables**, **S1 and S2 Figs**).

Bayesian Network models helped to understand the underlying structure of relationships between the molecular features. First, BN inference was used to explore how treatment response status

342 influences the probabilistic behavior of molecular descriptors. When the treatment resistance
343 node was fixed to either the sensitive or resistant state, the resulting shifts in marginal
344 probabilities revealed that treatment resistance exerts a structured, nonrandom influence on
345 specific network regions. The most strongly affected descriptors included the SASA (SD) for
346 G10 and E62, the SASA (AV) of H95, and LJ 1,4 energy (**Fig 5C**), aligning with the features
347 previously identified by ML models.

348 To assess whether these descriptors could, in turn, influence treatment response, each was fixed
349 to one of its discretized states, and the resulting marginal probabilities of the treatment resistance
350 node were computed. For comparison, 2 additional descriptors, the MSD of the binding site
351 backbone and the number of intraprotein hydrogen bonds, were also tested because they showed
352 little change during resistance-driven inference. This analysis revealed several nonlinear,
353 descriptor-specific effects. Specifically, reduced values of SASA for G10 (SD) and H95 (AV),
354 and increased values of SASA for E62 (SD) and LJ 1,4 energy, were associated with higher
355 marginal probabilities of treatment sensitivity (**Fig 5D**). Conversely, the opposite descriptor
356 states consistently shifted probabilities toward treatment resistance, reinforcing their importance
357 in shaping the resistance phenotype (**Fig 5D**). These findings are consistent with the ML results
358 regarding the molecular features distinguishing between the groups.

359 To visualize the features identified by ML models, the most populated MD conformations from
360 both treatment-sensitive and treatment-resistant KRAS systems were examined regarding the
361 residues G10, E62, and H95 conformations (**Fig 6**). Residues E62 and H95 exhibited distinct
362 conformational dynamics across the most populated clusters, which may explain the differences
363 in solvent exposure values and suggest potential alterations in ligand accessibility that warrant

364 further investigation. Residue G10 was located within a highly flexible region, where
365 neighboring residues likely contribute to the dynamic variability of its solvent exposure.

366 Overall, univariate statistical analysis and ML models (LR, RF, SVM, and BN) identified a
367 consistent set of molecular features that differed significantly between treatment-sensitive and
368 treatment-resistant systems. There was strong agreement across methods regarding feature
369 relevance, particularly for structural descriptors. The most influential features were
370 predominantly related to SASA within the switch II binding site. Across all ML models, the
371 SASA (SD) for G10 emerged as the top discriminatory feature, followed by the SASA (AV) of
372 H95, the SASA (SD) for E62, and LJ 1,4 energy. These findings highlight the central role of
373 residue-level flexibility, solvent exposure and nonbonded interactions in KRAS mutation-
374 induced drug resistance.

375 **Fig 6. Switch II binding-site dynamics.** Aligned most populated conformations from MD
376 simulations with important residues shown in sticks. (**A**) Side view. Residue A11 was removed
377 from the ML predictions because of high correlation with target variable and Q61 is known for
378 its catalytic activity. (**B**) Front view. The most important residues indicated by ML models (G10,
379 E62, and H95). Treatment-sensitive systems (KRAS G12C) in teal, treatment-resistant systems
380 (KRAS G12C/Y96C, KRAS G12C/Y96D, and KRAS G12C/Y96S) in salmon. Three examples
381 from each class are shown for clarity. Abbreviations: KRAS, Kirsten rat sarcoma viral oncogene
382 homolog; MD; ML, machine learning.

Discussion

In this study, the unit of biological variation was the KRAS variant; we analyzed four variants (G12C; G12C/Y96C, G12C/Y96S, G12C/Y96D) using 126 conformers from multiple PDB starts, replicas, and RMSD clusters, intentionally focusing on, although limited, yet clinically reported, resistance-associated double mutants within the inhibitor-binding site to provide hypothesis-generating results that we will expand with additional sensitive variants in future work. It is important to underline that all MD were performed in the unbound (apo) state; no complexes with inhibitors were simulated. Thus, any conclusions are restricted to conformational/topological shifts and do not establish inhibitor-specific resistance mechanisms. These unbound-state results motivate future testing with representative inhibitors but do not by themselves define resistance.

Our approach identified several residues (G10, K16, E62, and H95) as important contributors to treatment resistance in our models, consistent with their known roles in inhibitor recognition. For example, it has been shown that adagrasib forms a salt bridge with E62 and hydrogen bonds with H95 and K16, while its cyanomethyl group interacts with G10, displacing a conserved water molecule [17]. While sotorasib also forms hydrogen bonds with K16, it exploits a specific H95 orientation enhancing binding affinity to KRAS G12C, forms hydrogen bonds E63, and π- π interactions with Y96 [16]. Additionally, G10 solvation has been extensively discussed in previous structural and MD studies [17, 30, 41]. In our apo-state simulations, resistant systems showed increased solvent exposure of G10 and H95 residues and reduced flexibility of E62, suggesting altered solvation patterns and local rigidity around the binding site. These conformational features, even in the absence of ligand, pre-organize resistant mutants into states less compatible with optimal inhibitor binding.

406 Interestingly, while our ligand-free simulations of secondary resistant KRAS variants (e.g.,
407 G12C/Y96C/D/S) revealed mutation-dependent changes within the local contact network around
408 G10, K16, E62, and H95, independent ligand-bound MD studies have reported parallel shifts in
409 the contact frequencies of adagrasib and sotorasib with these same residues in mutants such as
410 G12C/R68S, G12C/K16T, G12C/Y96C, and G12C/Y96D [30], together supporting a model in
411 which resistance stems from subtle, mutation-induced conformational changes that pre-organize
412 the inhibitor-binding interface in the apo state and subsequently alter drug contacts upon binding.
413 In summary, we developed a framework that integrates computational chemistry methods with
414 machine learning algorithms, using KRAS mutation-induced resistance as a case study. Within
415 this framework, a dataset of comprehensive molecular descriptors, capturing structural,
416 energetic, thermodynamic, and contacts-based properties was derived from MD simulations and
417 analyzed by multiple methods. Predictive ML models, LR, RF, and SVM classified treatment
418 response based on molecular descriptors, while the BN revealed probabilistic dependencies
419 between features, enhancing interpretability. Together, these approaches identified subtle yet
420 meaningful differences in the dynamics of KRAS treatment-sensitive and treatment-resistant
421 systems, particularly in residue-level flexibility and solvent exposure. The conformational
422 behavior of key residues within the switch II binding site, as demonstrated in our results, could
423 be considered in the design of inhibitors for KRAS secondary mutants, resistant to sotorasib and
424 adagrasib, potentially improving therapeutic outcomes. Our study highlights the potential of ML
425 to address the complexity of mutation-induced drug resistance.
426 To date, the integration of protein flexibility or MD-derived features into ML models has not
427 been applied to problems as complex as mutation-induced drug resistance. Our approach
428 captures mutation-driven intrinsic conformational changes, not ligand-specific effects. This

429 reduces mechanism specificity but improves generalizability to other phenotypes and targets. By
430 incorporating protein dynamics before ligand-based analyses, it becomes possible to uncover
431 unique, targetable features that support the development of more selective and effective
432 inhibitors. Given the widespread impact of mutation-induced resistance across cancer types, we
433 propose extending this framework to other clinically relevant resistance-associated targets in the
434 future.

435 Methods

436 Computational chemistry

437 To investigate the dynamic behavior of KRAS mutants, we conducted all-atom MD simulations
438 of the inactive KRAS conformations bound to Mg^{2+} and GDP. The initial protein structures were
439 obtained from the Protein Data Bank (PDB) [42] under accession codes: 6OIM [17], 6UT0 [16],
440 and 6MBT [43], and prepared before MD simulations. For the KRAS G12C mutant bound to the
441 covalent inhibitor sotorasib (PDB ID: 6OIM), crystallographic water molecules were removed
442 together with the ligand. Missing amino acid residues 105-107 were reconstructed using
443 MODELLER 10.5 [44]. Three engineered mutations, C51S, C80L, and C118S [15], present in
444 the structure were reverted back to cysteines using the PyMOL 3.0 mutagenesis panel [40]. The
445 protein was capped with an acetyl group at the N-terminus and with a methyl amide at the C-
446 terminus using PyMOL's builder module [40]. This structure served as the basis for building
447 KRAS double mutant models, which have not yet been experimentally resolved. Subsequently,
448 KRAS G12C (PDB ID: 6OIM) was manually mutated in PyMOL to construct models of the
449 double mutants G12C/Y96C, G12C/Y96S, and G12C/Y96D. For the wild-type (WT) KRAS
450 structure (PDB ID: 6MBT) and the KRAS G12C mutant bound to the covalent inhibitor

451 adagrasib (PDB ID: 6UT0), the same preparation steps were applied. Additionally, the WT
452 KRAS structure was mutated at position 12, from glycine to cysteine, to model an additional
453 KRAS single-mutant system.

454 All protein models were processed using the CHARMM36 force field [45] in GROMACS [46].
455 Hydrogen atoms were added to each protein structure, and the protonation states of the residues
456 were assigned at neutral pH. The GDP molecule was parametrized separately with the
457 CHARMM General Force Field [47]. To prepare the systems for energy minimization, the
458 complexes were placed in cubic boxes, extending at least 10 Å from the protein. The solvent was
459 modeled using the CHARMM-modified TIP3P water model [45]. The protein charges were
460 neutralized by adding the appropriate amount of Na+ ions, and physiological NaCl salt
461 concentration 0.1M was ensured. Energy minimization was performed using the steepest descent
462 algorithm [48].

463 Next, NVT equilibration was conducted for 100 ps to stabilize the system's temperature at 310 K
464 with position restraints on protein and ligand heavy atoms to allow the solvent and ions to relax.
465 Temperature was maintained at 310 K using the V-rescale thermostat [49] with separate coupling
466 groups for protein and GDP ligand, and solvent/ions. H-bonds were constrained using LINCS
467 [50], enabling the 2 fs timestep. This was followed by 250 ps of NPT equilibration, continuing
468 from the NVT step, with the same position restraints and temperature control, while pressure was
469 maintained at 1 bar using isotropic Berendsen coupling [51]. Production MD were performed for
470 200 ns with a 2 fs timestep. Temperature was maintained at 310 K using the V-rescale
471 thermostat, and pressure was maintained at 1 bar using isotropic Parrinello-Rahman coupling.
472 Coordinates and energies were saved every 10 ps. Each system underwent 3 replica runs, with

473 different random seeds set before each simulation run. The water shell confirming octahedral
474 arrangement of water molecules around Mg^{2+} ion is shown in **S3 Fig**.

475 To extract representative conformations from the trajectories, we performed trajectory clustering
476 on the 50–200 ns portion of each simulation using the GROMOS [52] method. This method
477 counts neighboring structures within a specified cutoff and identifies the representative frame as
478 the one with the smallest average root mean square deviation (RMSD) to all its neighbors.
479 Clustering was performed for 6 different Cα RMSD cutoffs, ranging from 0.10 nm to 0.15 nm, to
480 find reasonable distribution of frames for each system. Representative structures from the top 7
481 clusters (~90% of the trajectory) were extracted from each of the 3 replicas per system for
482 molecular descriptors calculations. This resulted in 126 conformations across all 6 systems.
483 Specific elements of each system were treated separately in the calculations, including extended
484 switch II binding site residues (residues 9, 10, 11, 12, 16, 34, 35, 37, 58, 59, 60, 61, 62, 63, 64,
485 68, 69, 72, 95, 96, 99, 100, 102, and 103), which were defined as residues within 5Å of any site
486 point identified in the KRAS G12C switch II binding site by the SiteMap module [53, 54] of
487 Schrödinger Suite and included motifs from P-loop, switch I region, and adjacent helices. A full
488 list of molecular descriptors, grouped into categories, is provided in **Table 3**.

489 **Table 3. The complete list of the molecular descriptors extracted from MD simulations.**

Molecular dynamics simulation descriptors	
Calculation type	**System elements**
Structural descriptors	
Root Mean Square Deviation (RMSD, nm)*	Calculated as a function of time for: • protein backbone • switch II binding site residues (backbone and sidechains - heavy atoms) • GDP and protein backbone • Mg^{2+} ion and protein backbone
Radius of gyration (Rg, nm)*	Calculated as a function of time for (all-atoms): • protein • protein-GDP • switch II binding site residues
Root Mean Square Fluctuation (RMSF, nm)	Calculated per switch II binding site residue over the trajectory frames extracted for each cluster.
Solvent accessible surface area (SASA, nm^2) using the Double Cubic Lattice Method[55]	Total solvent accessible surface area, estimated solvation free energy, and total volume and density was calculated as a function of time for (all-atoms): • protein • switch II binding site residues

	Additionally, the average solvent accessible surface area and its standard deviation was calculated per each switch II binding site residue over the trajectory frames extracted from each cluster.
Mean Square Displacement (MSD, nm^2)	Calculated as a function of time for: • protein backbone • switch II binding site residues (backbone) • switch II binding site residues (sidechains-heavy atoms).
Energetic features	
Potential energy, total energy, kinetic energy, short-range and 1,4 Coulomb and Lennard-Jones (LJ) energies (kJ/mol)	Extracted for representative frame from the most populated conformational clusters.
Thermodynamic features	
Entropy estimate based on the quasiharmonic approach[56] and Schlitter's formula[57] (kJ/mol)	Estimated as an evolution of the system up to each cluster's representative timeframe.
Enthalpy (kJ/mol)	Extracted for representative frame from the most populated conformational clusters.
Intra- and intermolecular contacts	
Hydrogen bonds count	Calculated as a function of time for (all atoms): • within protein • between protein and GDP • within switch II binding site residues
Number of contacts within 6 Å	Calculated as a function of time for (heavy atoms): • between residue 12 and protein • between residue 12 and switch II binding site residues

*First frame of the production run was used as the reference conformation.

Statistical and ML methods

ML approach was implemented to identify the molecular descriptors distinguishing between treatment-sensitive and treatment-resistant KRAS mutants. The dataset consisted of 3 treatment-sensitive (resistance = 0) and 3 treatment-resistant (resistance = 1) KRAS systems, each contributing 63 samples, for a total of 126 samples described by 101 molecular features. To reduce redundancy, highly target-correlated and intercorrelated features (correlation >75%) were removed, along with all descriptors directly related to residue 96, the site of the secondary mutation, to avoid bias toward known changes. The remaining features were standardized using Z-score scaling to ensure comparable value ranges across inputs.

Before model training, we performed univariate statistical analysis. Feature distributions were tested for normality using the Shapiro–Wilk test [58], and the Mann–Whitney U test [59] was used to assess statistical significance between the feature data distribution in the treatment-sensitive and treatment-resistant groups. Violin plots [60, 61] were used to visualize feature

505 distributions, with central boxes indicating the interquartile range (IQR, 25th–75th percentile),
506 median lines, and whiskers extending 1.5× the IQR.

507 Since the relationships between features and resistance were not assumed to be strictly linear, 3
508 supervised ML models were applied: logistic regression (LR), random forest (RF), and support
509 vector machine (SVM), covering both linear and nonlinear classification paradigms.
510 Hyperparameter optimization was performed using GridSearchCV [62] with 5-fold cross-
511 validation. For LR, the L1 (Lasso), L2 (Ridge), and Elastic Net [62, 63] regularizations were
512 tested. The regularization strength C was varied (0.01, 0.1, 1, 10, 100) for all models,
513 while Elastic Net additionally included tuning of the l1_ratio (0.1, 0.5, 0.7, 1.0). For
514 the SVM classifier, the grid included C (0.01, 0.1, 1, 10, 100), kernel (linear, rbf, poly), gamma
515 (0.001, 0.01, 0.1, 1), and degree (2, 3, 4). For the RF model, the parameters tested
516 were n_estimators (50, 100, 150), max_depth (none, 10, 20), min_samples_split (2, 5,
517 10), min_samples_leaf (1, 2, 4), and max_features (sqrt, log2, none). Feature importance was
518 determined by using absolute coefficients for LR, total Gini impurity reduction for RF, and
519 permutation importance for SVM. Each model was trained on 80% of the data and tested on the
520 remaining 20%, with performance evaluated using 10-fold cross-validation to ensure
521 repeatability and prevent overfitting [63]. All analyses were conducted using Python 3.11.11[64].

522 To analyze probabilistic relationships among molecular descriptors, we used a Bayesian Network
523 (BN), an interpretable ML model that represents joint probability distributions as a directed
524 acyclic graph. A universal BN was constructed by combining treatment-sensitive and treatment-
525 resistant KRAS datasets using BNOmics [65], with 100 random restarts to ensure convergence
526 and structural robustness. Molecular descriptors were discretized into 3 categories, low (0),
527 medium (1), and high (2), using a maximum entropy algorithm [65]. The resulting network

528 captured both direct associations with treatment response and higher-order dependencies among
529 features. Two types of inference analyses were performed using a belief propagation algorithm.
530 First, to assess how treatment response affects molecular descriptors, the treatment resistance
531 node was fixed to either sensitive (0) or resistant (1), and the resulting posterior marginal
532 probabilities were computed for each feature. These distributions quantify how each node's
533 probability shifts in response to the fixed phenotype. Second, to evaluate how selected molecular
534 descriptors influence treatment response, each was fixed to one of its discretized states (0, 1, or
535 2), and the resulting marginal probability of the treatment resistance node was inferred. These
536 probabilities were compiled into a heatmap to visualize the effect of each perturbation.

537

539 # Data and code availability

540 The GitHub repository containing the code and data can be found at:

541 *https://github.com/Molecular-AI-Group/KatMizgalska/tree/KRAS-MD-descriptors*

542 # Author contributions

543 K.M. performed molecular dynamics simulations, conducted univariate statistical analyses and
544 predictive ML modeling and wrote and edited the manuscript. K.U. and S.B. performed and
545 described all analyses related to the BN. A.K designed the study in consultation with E.H., D.I.
546 and W.G., supervised it, and provided guidance on result interpretation and manuscript editing.
547 All authors reviewed and approved the final manuscript.

548 # Declaration of interests

549 Authors declare no conflicting interests.

550 # Funding

551 This research was supported in part by A.K. support funds and the National Institutes of Health
552 under grants R01-LM013138, and California Institute for Regenerative Medicine grant. CIRM
553 EDU4-12772, acknowledged by S.B. and K.U.

Acknowledgments

Molecular dynamics simulations were performed using HPC computing cluster at H. Lee Moffitt Cancer Center and Research Institute. Editorial assistance was provided by Moffitt Cancer Center's Office of Scientific Publishing by Gerard Hebert.

559 # References

560 1. Housman G, Byler S, Heerboth S, Lapinska K, Longacre M, Snyder N, et al. Drug
561 resistance in cancer: an overview. Cancers (Basel). 2014;6(3):1769–92.
562 2. Prahallad A, Sun C, Huang S, Di Nicolantonio F, Salazar R, Zecchin D, et al.
563 Unresponsiveness of colon cancer to BRAF(V600E) inhibition through feedback activation of
564 EGFR. Nature. 2012;483(7387):100–3.
565 3. Huang Y, Liu N, Liu J, Liu Y, Zhang C, Long S, et al. Mutant p53 drives cancer
566 chemotherapy resistance due to loss of function on activating transcription of PUMA. Cell
567 Cycle. 2019;18(24):3442–55.
568 4. Collet L, Hanvic B, Turinetto M, Treilleux I, Chopin N, Le Saux O, et al. BRCA1/2
569 alterations and reversion mutations in the area of PARP inhibitors in high grade ovarian cancer:
570 state of the art and forthcoming challenges. Front Oncol. 2024;14:1354427.
571 5. Yang Y, Zhang H, Huang S, Chu Q. KRAS Mutations in Solid Tumors: Characteristics,
572 Current Therapeutic Strategy, and Potential Treatment Exploration. J Clin Med. 2023;12(2).
573 6. Huang L, Guo Z, Wang F, Fu L. KRAS mutation: from undruggable to druggable in
574 cancer. Signal Transduct Target Ther. 2021;6(1):386.
575 7. Pantsar T. The current understanding of KRAS protein structure and dynamics. Comput
576 Struct Biotechnol J. 2020;18:189–98.
577 8. Bos JL, Rehmann H, Wittinghofer A. GEFs and GAPs: critical elements in the control of
578 small G proteins. Cell. 2007;129(5):865–77.
579 9. Li HY, Qi WL, Wang YX, Meng LH. Covalent inhibitor targets KRas(G12C): A new
580 paradigm for drugging the undruggable and challenges ahead. Genes Dis. 2023;10(2):403–14.
581 10. Tan AC, Tan DSW. Targeted Therapies for Lung Cancer Patients With Oncogenic Driver
582 Molecular Alterations. J Clin Oncol. 2022;40(6):611–25.

583 11. El Osta B, Behera M, Kim S, Berry LD, Sica G, Pillai RN, et al. Characteristics and
584 outcomes of patients with metastatic KRAS-mutant lung adenocarcinomas: the lung cancer
585 mutation consortium experience. J Thorac Oncol. 2019;14(5):876–89.
586 12. Parker JA, Mattos C. The K-Ras, N-Ras, and H-Ras Isoforms: Unique Conformational
587 Preferences and Implications for Targeting Oncogenic Mutants. Cold Spring Harb Perspect Med.
588 2018;8(8).
589 13. Blasco MT, Navas C, Martin-Serrano G, Grana-Castro O, Lechuga CG, Martin-Diaz L, et
590 al. Complete regression of advanced pancreatic ductal adenocarcinomas upon combined
591 inhibition of EGFR and C-RAF. Cancer Cell. 2019;35(4):573–87 e6.
592 14. Gibbs JB, Graham SL, Hartman GD, Koblan KS, Kohl NE, Omer CA, et al.
593 Farnesyltransferase inhibitors versus Ras inhibitors. Curr Opin Chem Biol. 1997;1(2):197–203.
594 15. Ostrem JM, Peters U, Sos ML, Wells JA, Shokat KM. K-Ras(G12C) inhibitors
595 allosterically control GTP affinity and effector interactions. Nature. 2013;503(7477):548–51.
596 16. Canon J, Rex K, Saiki AY, Mohr C, Cooke K, Bagal D, et al. The clinical KRAS(G12C)
597 inhibitor AMG 510 drives anti-tumour immunity. Nature. 2019;575(7781):217–23.
598 17. Fell JB, Fischer JP, Baer BR, Blake JF, Bouhana K, Briere DM, et al. Identification of
599 the Clinical Development Candidate MRTX849 , a Covalent KRAS ^{G12C}
600 Inhibitor for the Treatment of Cancer. Journal of Medicinal Chemistry. 2020;63(13):6679–93.
601 18. Zhang SS, Nagasaka M. Spotlight on sotorasib (AMG 510) for KRAS (G12C) positive
602 non-small cell lung cancer. Lung Cancer (Auckl). 2021;12:115–22.
603 19. Mahran R, Kapp JN, Valtonen S, Champagne A, Ning J, Gillette W, et al. Beyond
604 KRAS(G12C): biochemical and computational characterization of sotorasib and adagrasib
605 binding specificity and the critical role of H95 and Y96. ACS Chem Biol. 2024;19(10):2152–64.

606 20. Liu J, Kang R, Tang D. The KRAS-G12C inhibitor: activity and resistance. Cancer Gene
607 Ther. 2022;29(7):875–8.
608 21. Mohanty A, Nam A, Srivastava S, Jones J, Lomenick B, Singhal SS, et al. Acquired
609 resistance to KRAS G12C small-molecule inhibitors via genetic/nongenetic mechanisms in lung
610 cancer. Sci Adv. 2023;9(41):eade3816.
611 22. Ryan MB, Fece de la Cruz F, Phat S, Myers DT, Wong E, Shahzade HA, et al. Vertical
612 pathway inhibition overcomes adaptive feedback resistance to $KRAS^{G12C}$ inhibition. Clin Cancer
613 Res. 2020;26(7):1633–43.
614 23. Tanaka N, Lin JJ, Li C, Ryan MB, Zhang J, Kiedrowski LA, et al. Clinical acquired
615 resistance to $KRAS^{G12C}$ inhibition through a novel KRAS switch-II pocket mutation and
616 polyclonal alterations converging on RAS-MAPK reactivation. Cancer Discov.
617 2021;11(8):1913–22.
618 24. Rosen JC, Sacher A, Tsao MS. Direct GDP-$KRAS^{G12C}$ inhibitors and mechanisms of
619 resistance: the tip of the iceberg. Ther Adv Med Oncol. 2023;15:17588359231160141.
620 25. Koga T, Suda K, Fujino T, Ohara S, Hamada A, Nishino M, et al. KRAS secondary
621 mutations that confer acquired resistance to KRAS G12C inhibitors, sotorasib and adagrasib, and
622 overcoming strategies: insights from in vitro experiments. J Thorac Oncol. 2021;16(8):1321–32.
623 26. Awad MM, Liu S, Rybkin, II, Arbour KC, Dilly J, Zhu VW, et al. Acquired resistance to
624 $KRAS^{G12C}$ inhibition in cancer. N Engl J Med. 2021;384(25):2382–93.
625 27. Zhao Y, Murciano-Goroff YR, Xue JY, Ang A, Lucas J, Mai TT, et al. Diverse
626 alterations associated with resistance to $KRAS^{G12C}$ inhibition. Nature. 2021;599(7886):679–83.
627 28. Isermann T, Sers C, Der CJ, Papke B. KRAS inhibitors: resistance drivers and
628 combinatorial strategies. Trends Cancer. 2025;11(2):91–116.

629 29. Holderfield M, Lee BJ, Jiang J, Tomlinson A, Seamon KJ, Mira A, et al. Concurrent
630 inhibition of oncogenic and wild-type RAS-GTP for cancer therapy. Nature.
631 2024;629(8013):919–26.
632 30. Tu G, Liu Q, Qiu Y, Leung EL, Yao X. In Silico Study of the Acquired Resistance
633 Caused by the Secondary Mutations of KRAS G12C Protein Using Long Time Molecular
634 Dynamics Simulation and Markov State Model Analysis. Int J Mol Sci. 2022;23(22).
635 31. Pandey D, Roy KK. Decoding KRAS dynamics: Exploring the impact of mutations and
636 inhibitor binding. Arch Biochem Biophys. 2025;764:110279.
637 32. Mir SA, Nayak B, Aljarba NH, Kumarasamy V, Subramaniyan V, Dhara B. Exploring
638 KRas protein dynamics: an integrated molecular dynamics analysis of KRas wild and mutant
639 variants. ACS Omega. 2024;9(28):30665–74.
640 33. Mehmood A, Kaushik AC, Wang Q, Li CD, Wei DQ. Bringing structural implications
641 and deep learning–based drug identification for KRAS mutants. J Chem Inf Model.
642 2021;61(2):571–86.
643 34. Srisongkram T, Weerapreeyakul N. Drug Repurposing against KRAS Mutant G12C: A
644 Machine Learning, Molecular Docking, and Molecular Dynamics Study. Int J Mol Sci.
645 2022;24(1).
646 35. Stitou M, Koomen J, Imbody D, Liao Y, Monastyrskyi A, Rix U, et al. Does artificial
647 intelligence need companionship to assist in drug discovery? The Kirsten rat sarcoma virus
648 study. BJR Artif Intell. 2024;1(1).
649 36. Jamal S, Grover A, Grover S. Machine Learning From Molecular Dynamics Trajectories
650 to Predict Caspase-8 Inhibitors Against Alzheimer's Disease. Front Pharmacol. 2019;10:780.

651 37. Xia S, Chen E, Zhang Y. Integrated molecular modeling and machine learning for drug
652 design. J Chem Theory Comput. 2023;19(21):7478–95.
653 38. Cimermancic P, Weinkam P, Rettenmaier TJ, Bichmann L, Keedy DA, Woldeyes RA, et
654 al. CryptoSite: expanding the druggable proteome by characterization and prediction of cryptic
655 binding sites. J Mol Biol. 2016;428(4):709–19.
656 39. Meller A, Ward M, Borowsky J, Kshirsagar M, Lotthammer JM, Oviedo F, et al.
657 Predicting locations of cryptic pockets from single protein structures using the PocketMiner
658 graph neural network. Nat Commun. 2023;14(1):1177.
659 40. The PyMOL Molecular Graphics System, Version 3.0 Schrödinger, LLC.
660 41. Leini R, Pantsar T. In Silico Evaluation of the Thr58-Associated Conserved Water with
661 KRAS Switch-II Pocket Binders. J Chem Inf Model. 2023;63(5):1490–505.
662 42. Berman HM. The Protein Data Bank. Nucl Acids Res. 2000;28(1):235–42.
663 43. Dharmaiah S, Tran TH, Messing S, Agamasu C, Gillette WK, Yan W, et al. Structures of
664 N-terminally processed KRAS provide insight into the role of N-acetylation. Sci Rep.
665 2019;9(1):10512–.
666 44. Webb B, Sali A. Comparative Protein Structure Modeling Using MODELLER. Curr
667 Protoc Bioinformatics. 2016;54(1).
668 45. Huang J, Rauscher S, Nawrocki G, Ran T, Feig M, de Groot BL, et al. CHARMM36m:
669 an improved force field for folded and intrinsically disordered proteins. Nat Methods.
670 2017;14(1):71–3.
671 46. Van Der Spoel D, Lindahl E, Hess B, Groenhof G, Mark AE, Berendsen HJC.
672 GROMACS: fast, flexible, and free. J Comput Chem. 2005;26(16):1701–18.

673 47. Vanommeslaeghe K, Hatcher E, Acharya C, Kundu S, Zhong S, Shim J, et al. CHARMM
674 general force field: a force field for drug-like molecules compatible with the CHARMM all-atom
675 additive biological force fields. J Comput Chem. 2010;31(4):671–90.
676 48. William H. Press SAT, William T. Vetterling, Brian P. Flannery. Numerical Recipes in
677 FORTRAN: The Art of Scientific Computing: Cambridge University Press; 1986.
678 49. Bussi G, Donadio D, Parrinello M. Canonical sampling through velocity rescaling. J
679 Chem Phys. 2007;126(1).
680 50. Hess B. P-LINCS: a parallel linear constraint solver for molecular simulation. J Chem
681 Theory Comput. 2008;4(1):116–22.
682 51. Berendsen HJC, Postma JPM, van Gunsteren WF, DiNola A, Haak JR. Molecular
683 dynamics with coupling to an external bath. J Chem Phys. 1984;81(8):3684–90.
684 52. Daura XG, K. Jaun, B. Seebach, D. van Gunsteren, W. F., Mark AE. Peptide Folding:
685 When Simulation Meets Experiment. Angew Chem 1999;38:236–40.
686 53. Schrödinger Release 2024-3: SiteMap, Schrödinger, LLC, New York, NY, 2024.
687 54. Halgren TA. Identifying and characterizing binding sites and assessing druggability. J
688 Chem Inf Model. 2009;49(2):377–89.
689 55. Eisenhaber F, Lijnzaad P, Argos P, Sander C, Scharf M. The double cubic lattice method:
690 efficient approaches to numerical integration of surface area and volume and to dot surface
691 contouring of molecular assemblies. J Comput Chem. 1995;16(3):273–84.
692 56. Andricioaei I, Karplus M. On the calculation of entropy from covariance matrices of the
693 atomic fluctuations. J Chem Phys. 2001;115(14):6289–92.
694 57. Schlitter J. Estimation of absolute and relative entropies of macromolecules using the
695 covariance matrix. Chem Phys Lett. 1993;215(6):617–21.

58. Andrew P. King RJE. Chapter 7 – Inferential Statistics IV: Choosing a Hypothesis Test. Andrew P. King RJE, editor: Academic Press; 2019.

59. Nachar N. The Mann-Whitney U: a test for assessing whether two independent samples come from the same distribution. Tutor Quant Methods Psychol. 2008;4(1):13–20.

60. Waskom M. Seaborn: statistical data visualization. J Open Source Softw. 2021;6(60).

61. Hunter JD. Matplotlib: a 2D graphics environment. Comput Sci Eng. 2007;9(3):90–5.

62. Pedregosa F, Varoquaux G, Gramfort A, Michel V, Thirion B, Grisel O, et al. Scikit-learn: machine learning in python. J Mach Learn Res. 2011;12(null):2825–30.

63. Gareth JW, D.; Hastie, T.; Tibshirani, R.;. An Introduction to Statistical Learning: Springer; 2013.

64. Van Rossum G, Drake FL. Python 3 Reference Manual: CreateSpace; 2009.

65. Gogoshin G, Boerwinkle E, Rodin AS. New algorithm and software (BNOmics) for inferring and visualizing Bayesian Networks from heterogeneous big biological and genetic data. J Comput Biol. 2017;24(4):340–56.

Supporting Information

S1 Table. XGBoost model evaluation.

S2 Table. PLS-DA model evaluation.

S1 Fig. XGBoost model performance. Left: XGBoost ROC-AUC across 10 iterations. Right: top 15 Feature Importance averaged over 10 iterations calculated using a Permutation technique. This model, even after small-data set adjustment, still relies on one dominant feature SASA (SD) of G10. It agrees with the models studied in the publication.

S2 Fig. PLS-DA model performance. Left: PLS-DA ROC-AUC across 10 iterations. Right: top 15 Feature Importance averaged over 10 iterations calculated using a Variable Importance in Projection (VIP) scores, which estimate each feature contribution to the production. This model does not rely heavily on a few features, but consensus between several equally important. The result agrees with the models studied in the publication.

S3 Fig. Water shell around Mg^{2+}. Left: initial structure (PDB ID: 6OIM, X-ray crystallography). Right: system's starting structure after the NPT equilibration ready for the simulation run.

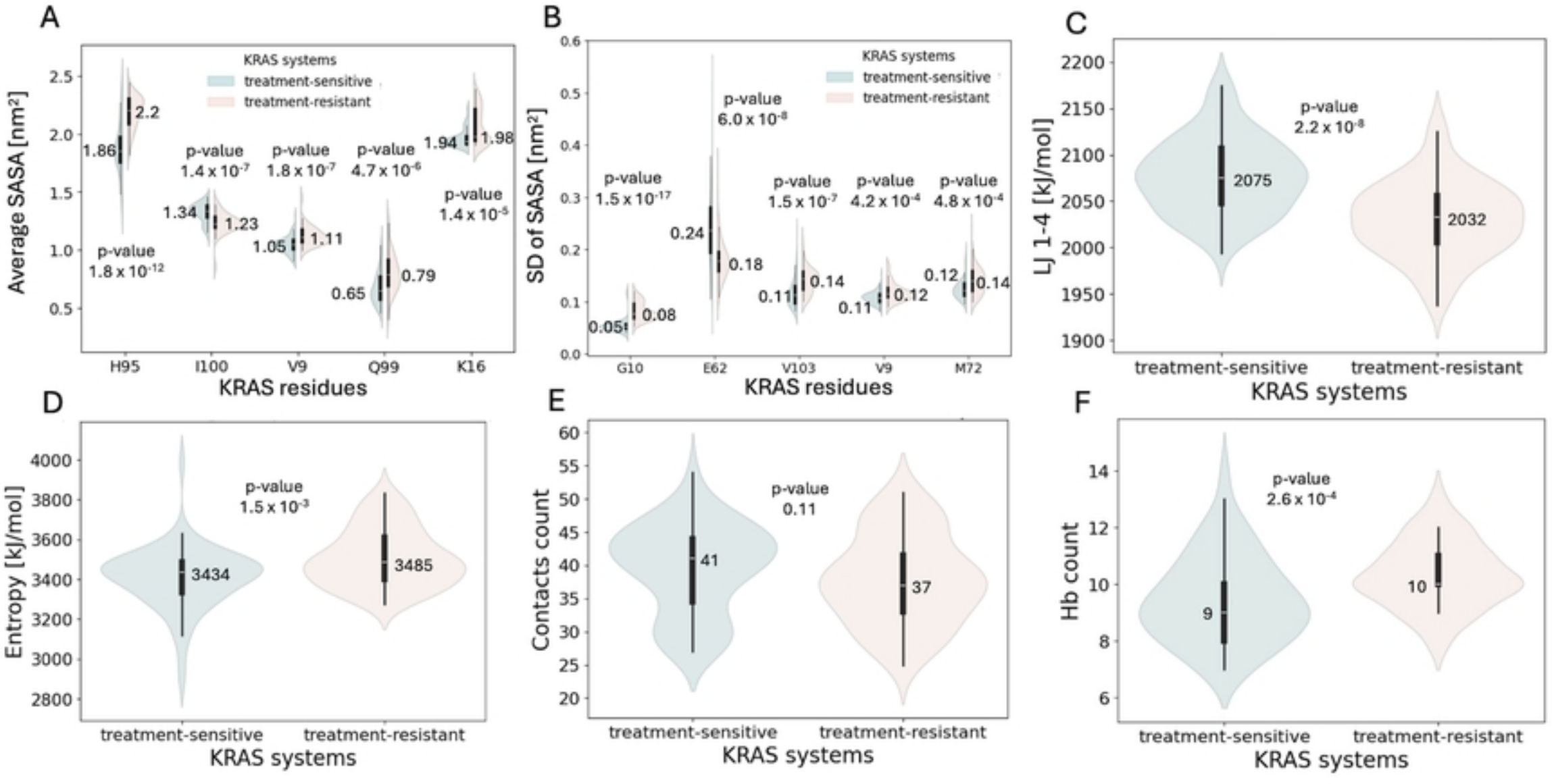
A
KRAS systems
treatment-sensitive
treatment-resistant
Average SASA [nm²]
2.5
2.0
1.5
1.0
0.5
1.86
2.2
p-value
1.8 x 10-12
1.34
1.23
p-value
1.4 x 10-7
1.05
1.11
p-value
1.8 x 10-7
0.65
0.79
p-value
4.7 x 10-6
1.94
1.98
p-value
1.4 x 10-5
H95
I100
V9
Q99
K16
KRAS residues
B
KRAS systems
treatment-sensitive
treatment-resistant
SD of SASA [nm²]
0.6
0.5
0.4
0.3
0.2
0.1
0.0
p-value
1.5 x 10-17
0.05
0.08
p-value
6.0 x 10-8
0.24
0.18
p-value
1.5 x 10-7
0.11
0.14
p-value
4.2 x 10-4
0.11
0.12
p-value
4.8 x 10-4
0.12
0.14
G10
E62
V103
V9
M72
KRAS residues
C
LJ 1-4 [kJ/mol]
2200
2150
2100
2050
2000
1950
1900
p-value
2.2 x 10-8
2075
2032
treatment-sensitive
treatment-resistant
KRAS systems
D
Entropy [kJ/mol]
4000
3800
3600
3400
3200
3000
2800
p-value
1.5 x 10-3
3434
3485
treatment-sensitive
treatment-resistant
KRAS systems
E
Contacts count
60
55
50
45
40
35
30
25
20
p-value
0.11
41
37
treatment-sensitive
treatment-resistant
KRAS systems
F
Hb count
14
12
10
8
6
p-value
2.6 x 10-4
9
10
treatment-sensitive
treatment-resistant
KRAS systems

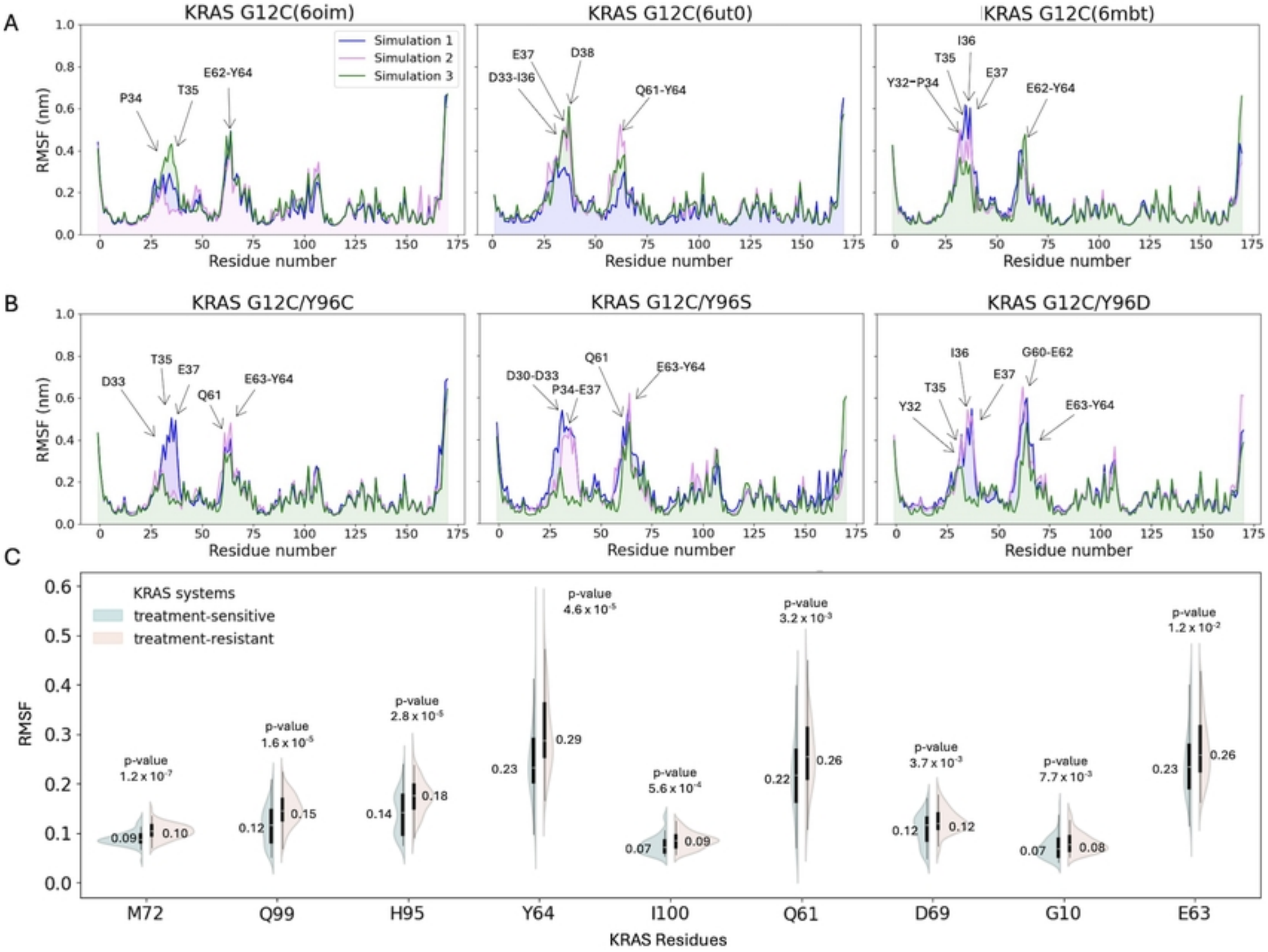
A
KRAS G12C(6oim)
KRAS G12C(6ut0)
KRAS G12C(6mbt)
Simulation 1
Simulation 2
Simulation 3
RMSF (nm)
Residue number
P34
T35
E62-Y64
E37
D38
D33-I36
Q61-Y64
I36
T35
E37
Y32-P34
E62-Y64
B
KRAS G12C/Y96C
KRAS G12C/Y96S
KRAS G12C/Y96D
D33
T35
E37
Q61
E63-Y64
D30-D33
P34-E37
Q61
E63-Y64
I36
G60-E62
E37
T35
Y32
E63-Y64
C
KRAS systems
treatment-sensitive
treatment-resistant
RMSF
p-value 1.2 x 10-7
p-value 1.6 x 10-5
p-value 2.8 x 10-5
p-value 4.6 x 10-5
p-value 5.6 x 10-4
p-value 3.2 x 10-3
p-value 3.7 x 10-3
p-value 7.7 x 10-3
p-value 1.2 x 10-2
M72
Q99
H95
Y64
I100
Q61
D69
G10
E63
KRAS Residues

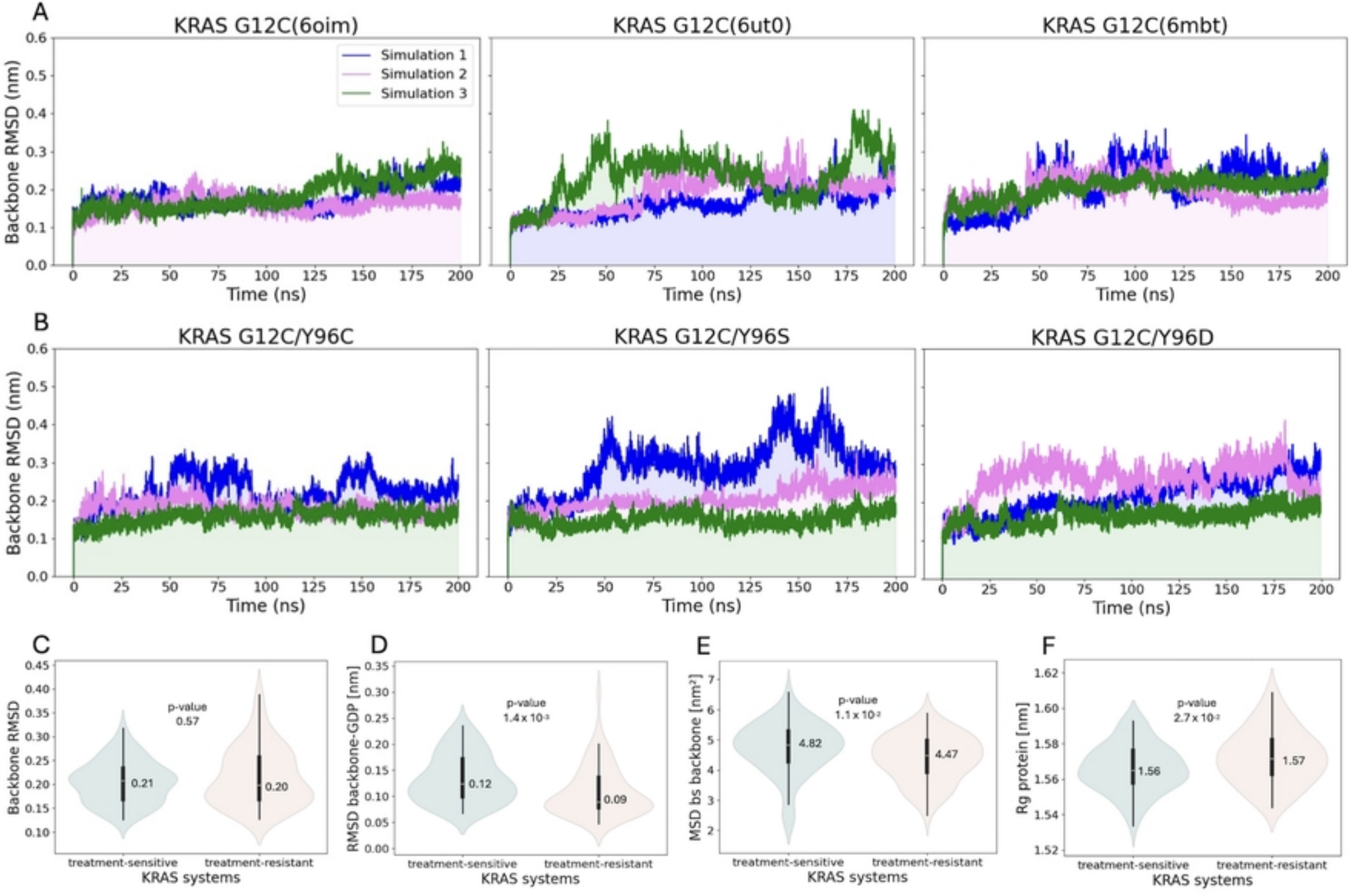
A
KRAS G12C(6oim)
KRAS G12C(6ut0)
KRAS G12C(6mbt)
Simulation 1
Simulation 2
Simulation 3
Backbone RMSD (nm)
Time (ns)
B
KRAS G12C/Y96C
KRAS G12C/Y96S
KRAS G12C/Y96D
C
Backbone RMSD
p-value
0.57
0.21
0.20
treatment-sensitive
treatment-resistant
KRAS systems
D
RMSD backbone-GDP [nm]
p-value
1.4 x 10-3
0.12
0.09
E
MSD bs backbone [nm²]
p-value
1.1 x 10-2
4.82
4.47
F
Rg protein [nm]
p-value
2.7 x 10-2
1.56
1.57

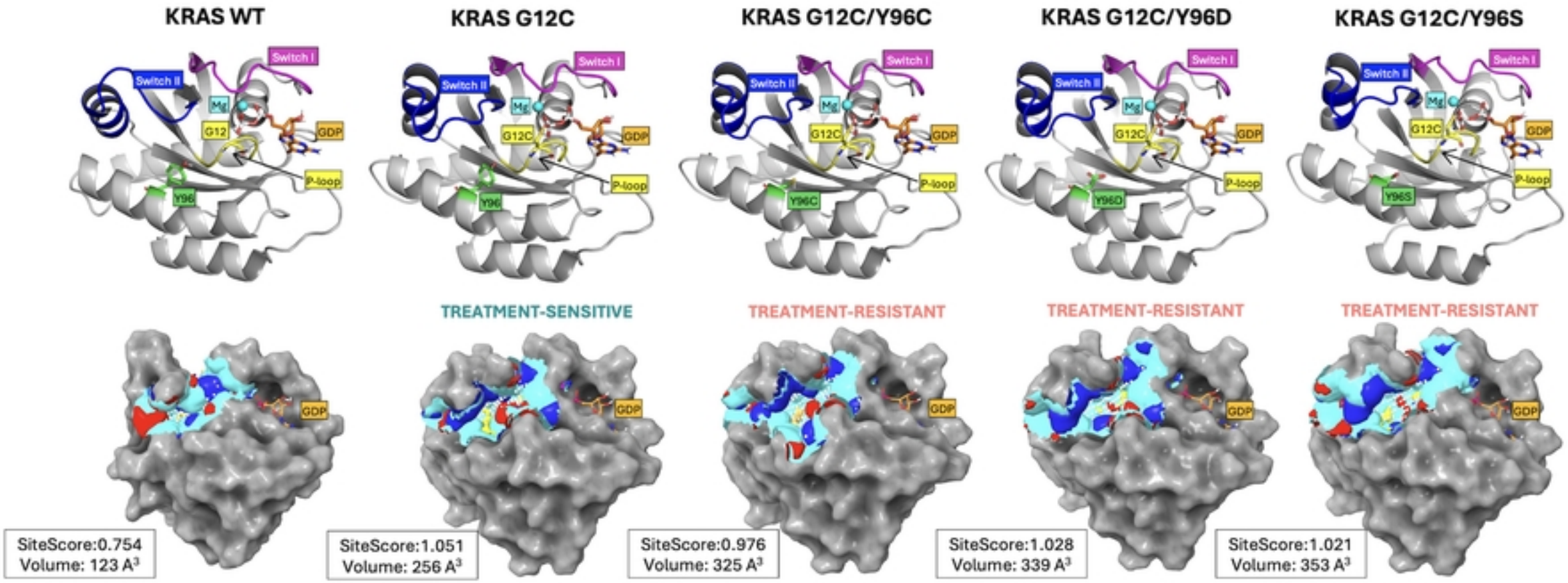
KRAS WT
KRAS G12C
KRAS G12C/Y96C
KRAS G12C/Y96D
KRAS G12C/Y96S
Switch I
Switch II
Mg
G12
G12C
GDP
P-loop
Y96
Y96C
Y96D
Y96S
TREATMENT-SENSITIVE
TREATMENT-RESISTANT
TREATMENT-RESISTANT
TREATMENT-RESISTANT
SiteScore:0.754
Volume: 123 A³
SiteScore:1.051
Volume: 256 A³
SiteScore:0.976
Volume: 325 A³
SiteScore:1.028
Volume: 339 A³
SiteScore:1.021
Volume: 353 A³

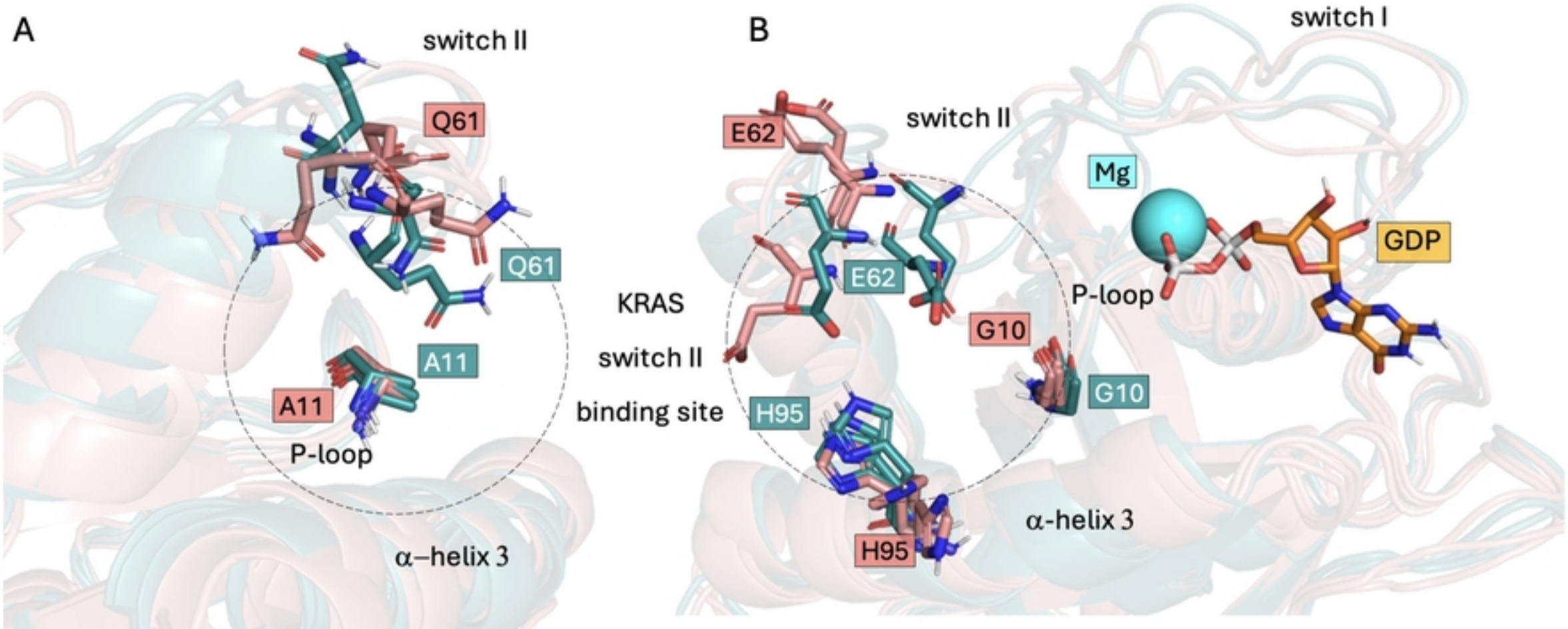
A
switch II
Q61
Q61
A11
A11
P-loop
α–helix 3
KRAS
switch II
binding site
B
switch I
switch II
E62
E62
Mg
GDP
P-loop
G10
G10
H95
H95
α-helix 3

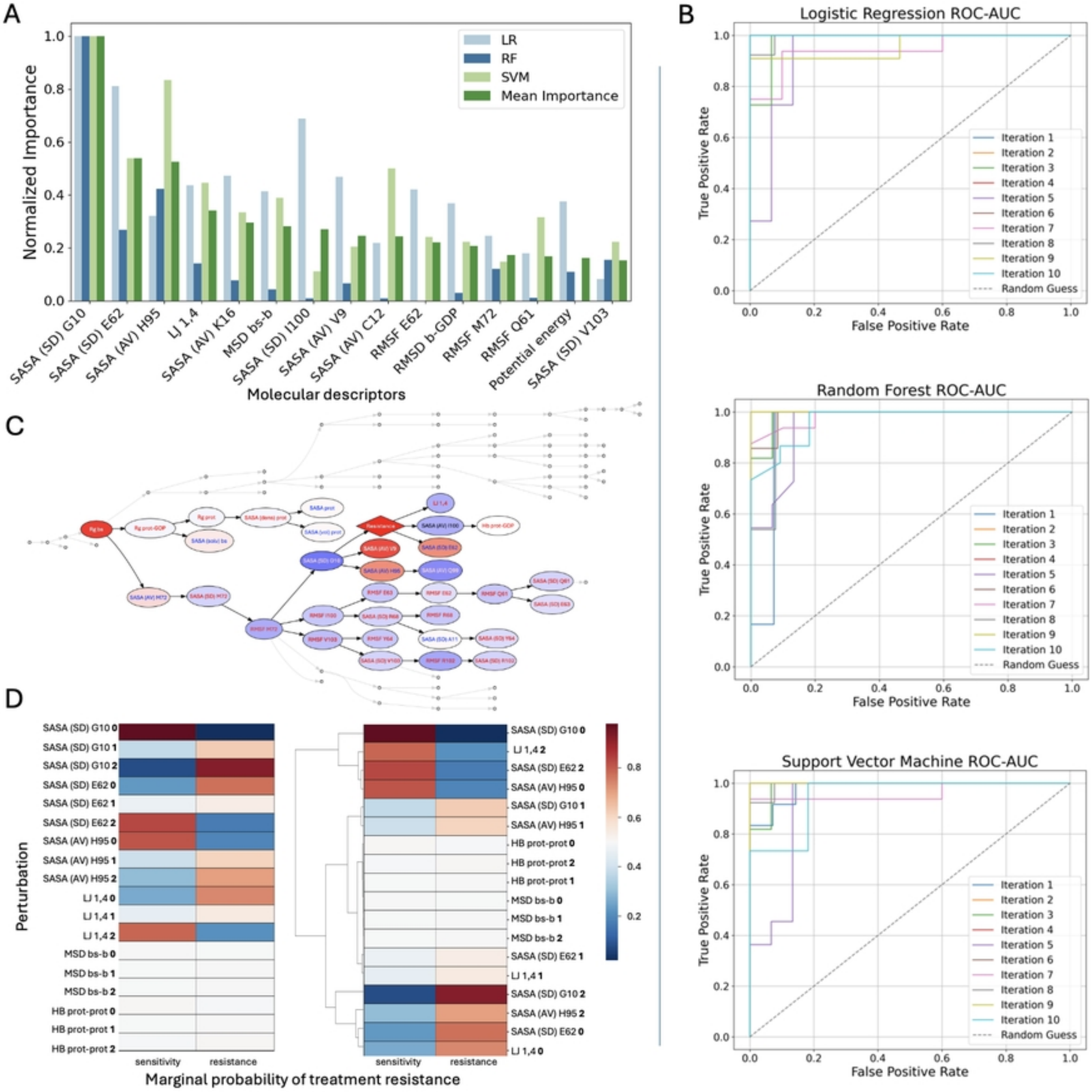
A
Normalized Importance
LR
RF
SVM
Mean Importance
SASA (SD) G10
SASA (SD) E62
SASA (AV) H95
LJ 1,4
SASA (AV) K16
MSD bs-b
SASA (SD) I100
SASA (AV) V9
SASA (AV) C12
RMSF E62
RMSD b-GDP
RMSF M72
RMSF Q61
Potential energy
SASA (SD) V103
Molecular descriptors
B
Logistic Regression ROC-AUC
True Positive Rate
False Positive Rate
Iteration 1
Iteration 2
Iteration 3
Iteration 4
Iteration 5
Iteration 6
Iteration 7
Iteration 8
Iteration 9
Iteration 10
Random Guess
C
D
Perturbation
sensitivity
resistance
Marginal probability of treatment resistance
Random Forest ROC-AUC
Support Vector Machine ROC-AUC